Contents lists available at ScienceDirect

Computers and Geosciences

journal homepage: www.elsevier.com/locate/cageo

Research paper

Numerical stratigraphic forward models as conceptual knowledge repositories and experimental tools: An example using a new enhanced version of CarboCAT

Isabella Masiero [a,*], Estanislao Kozlowski [b], Georgios Antonatos [b], Haiwei Xi [a], Peter Burgess [a]

[a] Quantitative Experimental Stratigraphy Group, Jane Herdman Laboratory, Department of Earth, Ocean and Ecological Science, University of Liverpool, Brownlow Street, Liverpool L69 3GP, UK

[b] Department of Earth Sciences, Royal Holloway, University of London, Egham, TW20 0EX, UK

ARTICLE INFO

Keywords:
Carbonates
Stratigraphic forward modelling
Syn-rift carbonates

ABSTRACT

A new, enhanced version of the CarboCAT numerical stratigraphic forward model includes additional cross-platform and down-slope, event-based sediment transport, pelagic carbonate production and deposition, wave-energy calculations and facies sensitivity, and fault-controlled tectonic subsidence. Simple testing of this new version against observed and conceptual models of fault-controlled carbonate platform deposition suggests that the new model formulation is both realistic and useful for either data-constrained best-fit modelling or numerical experiments to explore how carbonate depositional systems produce strata.

1. Introduction

Numerical stratigraphic forward models are increasingly important, as a repository of what we understand about how sediment is produced, transported and how it accumulates to create heterogeneous strata (Burgess, 2012; Paola, 2000). Two basic modes of modelling are typically used. In one mode, numerical stratigraphic forward models make predictions away from the points where the model is constrained by data, and the information contained in the modelled processes and the initial conditions lead to hopefully useful predictions away from those data points (e.g. Lanteaume et al., 2018; Warrlich et al., 2008; Wilson et al., 2000). In the second mode, numerical stratigraphic forward models are used in more experimental mode, to explore the validity and consequences of various geological hypothesis and assumptions (e.g. Burgess et al., 2019; Williams et al., 2011; Burgess, 2006; Warrlich et al., 2002; Burgess et al., 2001). Used either way, numerical stratigraphic models are a significantly important step beyond cartoon conceptual models (Burgess, 2012).

CarboCAT is a 3D numerical stratigraphic forward model of carbonate depositional systems, first developed and described in Burgess (2013). CarboCAT is a reduced complexity model (e.g. Brasington and Richards, 2007) that models carbonate sediment production, transport and accumulation under various tectonic and eustatic settings. CarboCAT uses a detailed event-based approach to production, transport and deposition, creating a potentially realistic bed-scale representation of heterogeneous carbonate strata. Complex variations in production are modelled using a deterministic cellular automata (CA) approach (e.g. Wolfram, 2002) to simulate spatial competition between multiple carbonate factories (sensu Schlager, 2005), producing significant heterogeneity in the resulting strata, as observed in real deposits (e.g. Wright and Burgess, 2005). CarboCAT also simulates sediment redistribution by various processes, including both cross platform transport and down-slope transport that can produce event deposits in basinal lows. CarboCAT cell elements can have any size, so a modelled factory present in one model cell could represent the work of a limited group of organisms or a more diverse, larger-scale carbonate factory with multiple organisms (sensu Schlager, 2005).

CarboCAT (Burgess, 2013) has been improved and developed progressively through four doctoratal projects (Antonatos, 2018; Kozlowski, 2016; Masiero, in prep.; Haiwei, in prep.). New CarboCAT elements include fault controlled spatially and temporally variable subsidence, wind-induced wave propagation and wave-energy controlled facies development, cross-platform current and down-slope gravity-driven sediment transport processes, and siliciclastic sediment input, transport and interaction with carbonate production. Upgraded CarboCAT can now model mixed carbonate–siliciclastic depositional systems in active syn-rift settings, with complex eustatic forcing and wave control, and complex redistribution of produced sediment across a range of possible platform types.

This paper: (1) provides a complete description and specification of this new improved version of CarboCAT; (2) demonstrates how

* Corresponding author.
E-mail address: isabella.masiero@liverpool.ac.uk (I. Masiero).

https://doi.org/10.1016/j.cageo.2020.104453
Received 11 September 2019; Received in revised form 3 February 2020; Accepted 18 February 2020

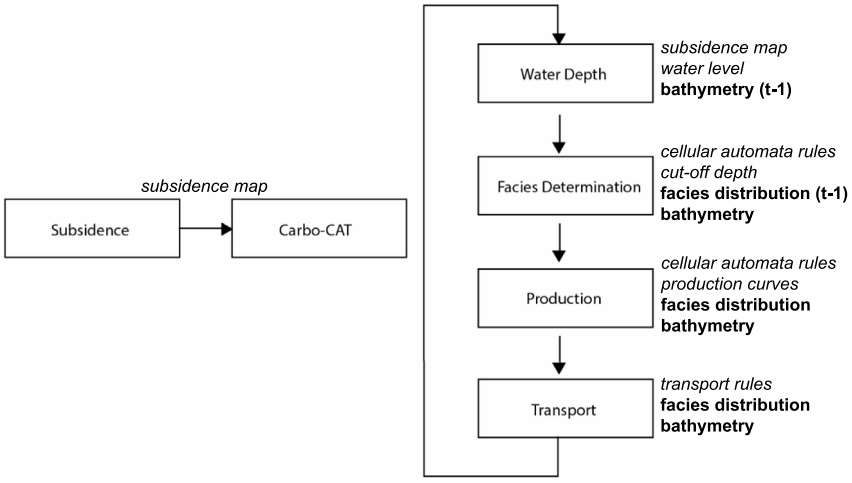

Fig. 1. Rationale of CarboCAT algorithm including principal subroutines. In italic: user-defined input parameters used in each process. In bold: modelled variables used in each process.
Source: From Kozlowski (2016).

numerical stratigraphic models can be a repository for established ideas about depositional system functioning. New CarboCAT models replicate existing conceptual models of syn-rift carbonate platforms, testing the validity of our understanding of governing geological processes in this tectonic setting.

1.1. Model basics

CarboCAT algorithm works on a regular x, y, t grid where x and y are the planform map dimensions and t is the elapsed model time. The model grid does not have an explicit scale, and the model cell size is defined by the user. For every model iteration, CarboCAT executes a specific series of operations to simulate tectonic subsidence and uplift, sea-level change, carbonate production, and sediment transport and re-deposition (Fig. 1).

1.2. Regional and fault-related differential subsidence

The new version of CarboCAT simulates differential subsidence across extensional normal faults. A fault-controlled subsidence field is calculated a priori (Fig. 1), either constant or varying through time, that is used to calculate the subsidence value affecting every model grid cell, at every iteration during the principal CarboCAT run. Existing stratigraphic forward models such as Sedsim (Griffiths et al., 2001), Sedpak (Csato and Kendall, 2002) and Dionisos (Aschoff and Rountree, 2012) incorporate simple subsidence models, relying on the definition of subsidence maps to model spatially variable subsidence.

In CarboCAT, multiple faults can be modelled, with a broad number of input parameters controlling each fault orientation and dip angle, geometry and associated kinematic behaviour (Fig. 2a). Initial and final fault length, L, defines various scenarios of fault evolution (Schlagenhauf et al., 2008; Morley et al., 2007) that range from fault nucleation, when initial length is set to zero, to reactivation of inherited structures, when initial length, and possibly displacement, are larger than zero. Maximum deformation direction is always perpendicular fault strike. Beginning and termination of fault activity, and the accumulated hanging-wall subsidence, h_{HW}, are input values that determine rate of fault slip.

Additional parameters control footwall uplift, h_{FW}, occurring at different rates and magnitudes than the hanging wall subsidence, representing flexural isostacy and co-seismic uplift (e.g. Jackson and McKenzie, 1988). Hanging wall and footwall deformation can vary away from the fault in either a linear or quadratic way to represent planar or listric faults, respectively. In both cases maximum displacement is directly adjacent to the fault, decreasing to zero at a given distance, defining the hanging-wall, L_{HW}, and footwall, L_{FW}, block dip length. Extent of fault-plane orthogonal deformation may be constant as the fault grows, with a fixed hinge point over hanging-wall and footwall blocks to represent rotational faulting (e.g. 'domino' structures). Alternatively, fault extent can increase through time, migrating hinge points away from the fault plane and progressively increasing fault block dip lengths.

Depocenter position, and fault plane shape can be controlled with the *asymmetric index*, an input parameter controlling fault plane geometry, which can be rectangular if the fault displacement is constant along-strike, triangular when displacement decreases linearly towards the fault tips, or curved following a quadratic relationship. Displacement rate may be constant, accelerating or decelerating through time.

The main limitation of the fault subsidence routine concerns fault dip. Compared to more complex approaches (e.g. Waltham and Hardy, 1995), CarboCAT uses an orthogonal grid with equidimensional cells and constant x, y grid point location, limiting resolution of cumulative horizontal displacement of dipping faults to the model cell dimension (Fig. 2b–c). Despite this limitation, CarboCAT fault model is sufficient to explore how different extensional fault configurations may affect carbonate stratal geometries in three dimensions due to differential accommodation, topographic development and flow-routing (e.g. Cross and Bosence, 2008; Leeder and Gawthorpe, 1987).

1.3. Carbonate facies distribution and production

CarboCAT models a maximum of four, different in-situ carbonate facies. In-situ produced facies for each model simulation are defined by user-defined input parameters that determine spatial distribution, production rate, and proportion of produced thickness that can be removed and redistributed by sediment transport mechanisms. The spatial distribution of carbonate facies at each model time step iteration is calculated using a cellular automata algorithm (Fig. 3) and the thickness of sediment produced in each cell at each time step is calculated using a maximum production rate, modified by a production rate depth curve (e.g. ? Bosscher and Schlager, 1992; Bosence and Waltham, 1990) which may be different for each carbonate facies type. Facies occurrence is also controlled by wave energy, limiting facies appearance to areas where energy levels are within a maximum and a minimum values specified by the user for each wave-sensitive carbonate facies. When the latter condition is met, carbonate accumulation rates are not directly influenced by wave energy, however, future CarboCAT developments will address this limitation.

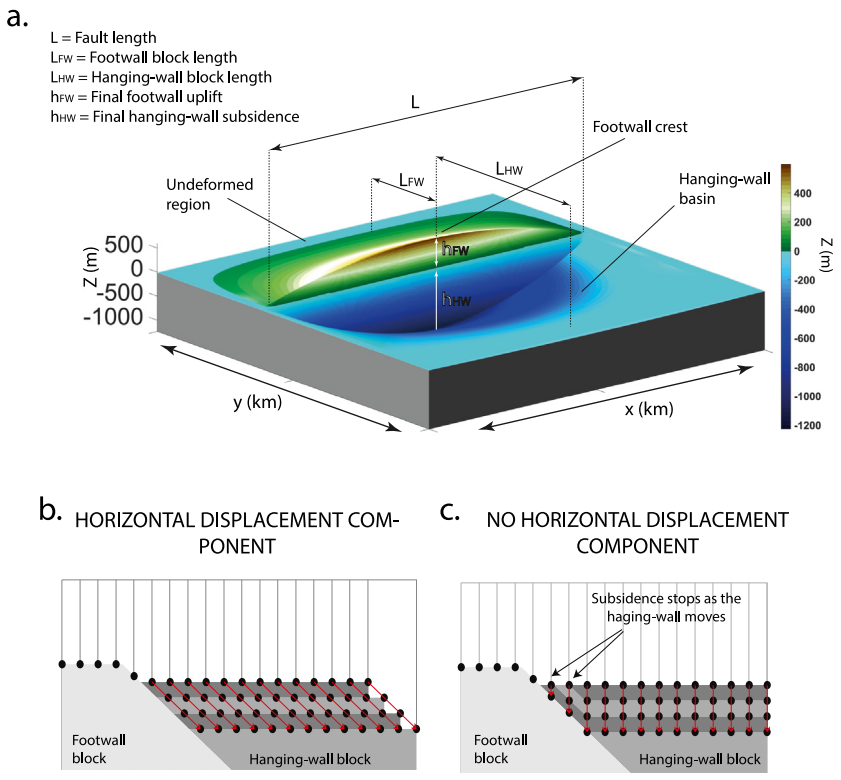

Fig. 2. a. CarboCAT model representing isolated normal fault with symmetric displacement showing main geometrical input parameters. b.,c. two methods for modelling hanging-wall deformation in normal faults. In b., the horizontal component of the hanging-wall displacement is represented and grid point position $x-y$ changes with increasing deformation; in c., fault modelling approach implemented in CarboCAT: only vertical deformation is represented and subsidence is not continuously created as the hanging-wall moves. The latter approach is computationally more efficient since the grid point position $x-y$ is fixed. However, the effect on strata of normal faulting with horizontal displacement exceeding horizontal cell size may not be adequately represented.
Source: Modified from Kozlowski (2016).

1.3.1. Carbonate spatial distribution by cellular automata

CarboCAT simulates production of spatially heterogeneous carbonate facies by multiple carbonate producing organisms or factories using a deterministic cellular automata (CA) algorithm (e.g. Wolfram, 2002). Widely used in the modelling of biological system dynamics (e.g. Flake, 1998; Clarke et al., 1997; Silvertown et al., 1992), the CA approach allows simulation of complex dynamic behaviour arising on a simple model grid due to interaction of multiple carbonate producers, from single species to whole factories, depending on the grid cell scale. Depending on defined model resolution, each facies grid cell may represent production by a single type of organism, for high resolution model grids with cell size in the order of tens of meters, or a broader association of organisms within a carbonate factory (Schlager, 2000; Pomar and Hallock, 2008), for low resolution models with cell size in the order of hundreds of meters. Population of each grid cell is determined by application of simple rules based on a count of same-type neighbours in adjacent cells across a specified area (Fig. 3a.,b. and c.). This represents competition for space and nutrients and can generate realistically heterogeneous carbonate strata even with simple rules (Fig. 3d.).

1.3.2. Carbonate shallow-water benthic production rates

Once facies spatial distribution for a time step has been determined, carbonate volume produced at every grid cell E is calculated with:

$$E(x,y) = e_{x,y} \cdot ts \cdot R_{x,y} \tag{1.3.1}$$

where e is the accumulation rate based on Bosscher and Schlager (1992), ts is the time step and R is the production rate modifier, a coefficient that weights the production associated to a certain facies by scaling it to the number of cells occupied by the same type of facies in the surrounding neighbourhood (Fig. 4a.). Assuming that growth rate is linked to the ability of carbonate producers to remain healthy, the maximum production (i.e. $R = 1$) will be achieved in cells with the optimum amount of same-facies neighbours ($n_{optimum}$).

The accumulation rate e is calculated through:

$$e(x,y) = e_m \cdot \tanh \frac{I_0 e^{-k_e w}}{I_k} \tag{1.3.2}$$

where e_m is the maximum accumulation rate for the facies occupying x, y cell, I_0 and I_k are the surface and saturating light intensities, k_e is the extinction coefficient and wd is the water depth at cell x, y. These parameters represent different type of factories, for example euphotic or oligophotic (Fig. 4b.).

1.3.3. Pelagic production

Pelagic carbonates are produced through a range of water depth and light conditions. Therefore, pelagic accumulation rate P in any x, y cell is proportional to water column height above that cell, calculated through the following equation (proposed by Bosence and Waltham, 1990):

$$P(x,y) = P_{max} \cdot (1 - exp(-\frac{wd(x,y)}{p_f})) \tag{1.3.3}$$

where P_{max} is maximum production rate for pelagic, $wd(x,y)$ is water depth and p_f is an exponential decay factor.

Pelagic sediment accumulation occurs where wave energy and current shear stress are zero, so typically deep-water, low-energy basinal locations where fine particles can settle.

1.4. Sediment redistribution mechanisms

Entrainment, transport, and redeposition of in-situ produced carbonate sediment in CarboCAT are calculated as discrete events, several

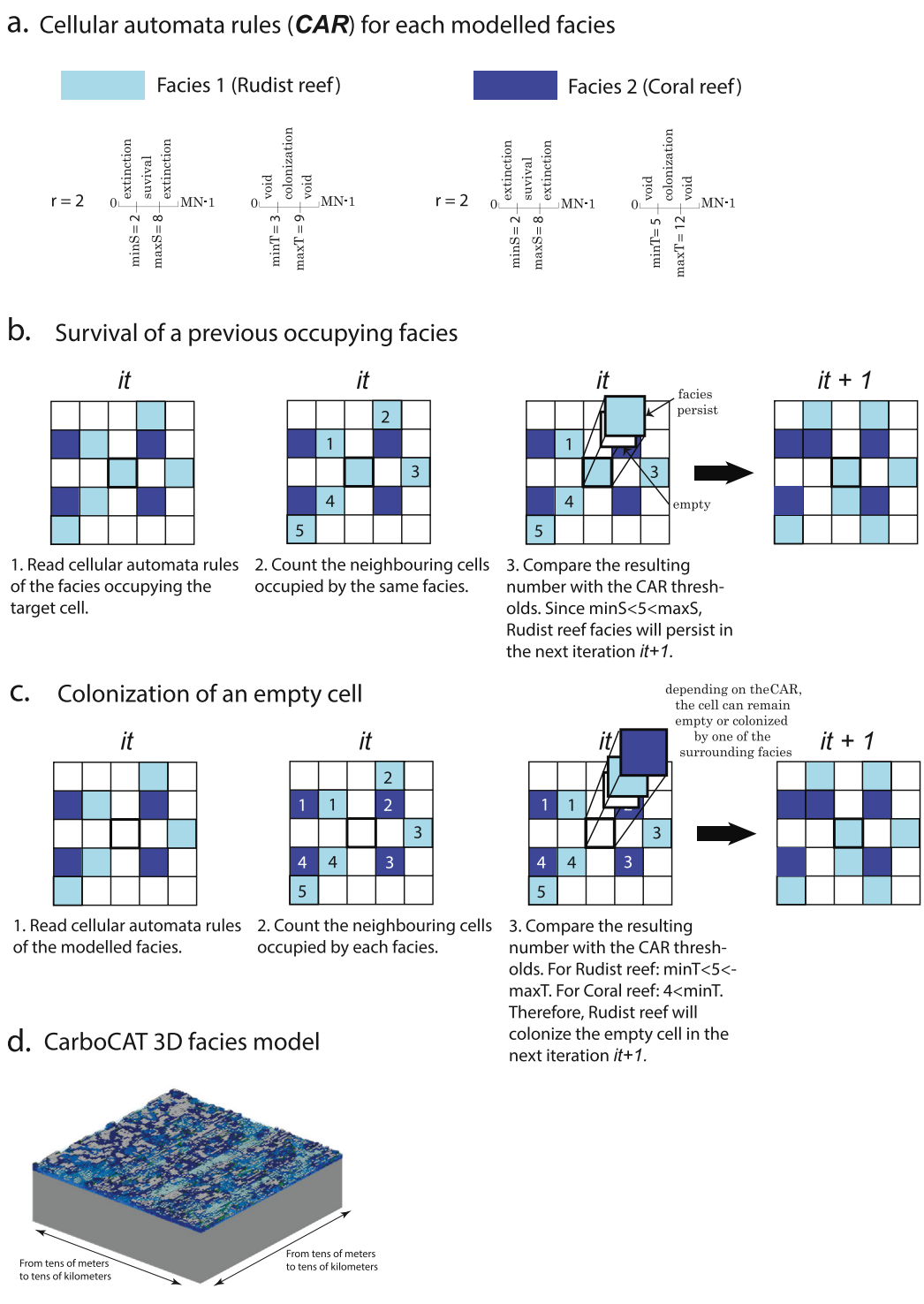

Fig. 3. The cellular automata algorithm used in CarboCAT. a. cellular automata rules (CAR) defined by the user for each modelled facies (in the example rudist reef and coral reef) to simulate factories dynamics. The radius r controls the numbers of cells to use in the cellular automata. The minimum and maximum survival values ($minS$ and $maxS$) determine the minimum and maximum number of neighbouring cells colonized by the same facies that are required for the facies to survive in the next iteration ($it + 1$). The minimum and maximum triggering values ($minT$ and $maxT$) control whether a cell empty in the current iteration (it) will be occupied by a producing factory in the next iteration ($it + 1$). CA rules values are limited by the Moore neighbourhood (MN) that represents the number of surrounding cells within the defined radius r. b.-c. Set of operations (1–3) performed by the cellular automata algorithm at any model iteration (it) when b. facies occupying a certain cell in the model grid survives to the next iteration ($it + 1$) and c. an empty cell is colonized by one of the neighbouring facies. d. Simple CarboCAT 3D stratigraphic model result.

in each model iteration. This generates a realistic, bed-scale facies heterogeneity. Each in-situ produced facies has a defined median grain diameter, D_{50}, and a threshold grain size, D_T, that determine if transport occurs as bed load or suspended load. Suspended particles are always transported by currents, while bedload transport and deposition can be either current-driven (Fig. 5) or gravity-driven, following an approach originally proposed by Warrlich et al. (2002), and recently used by Salles et al. (2018). CarboCAT has open grid boundary conditions, allowing transported sediment to leave the model domain without generating unrealistic edge effects.

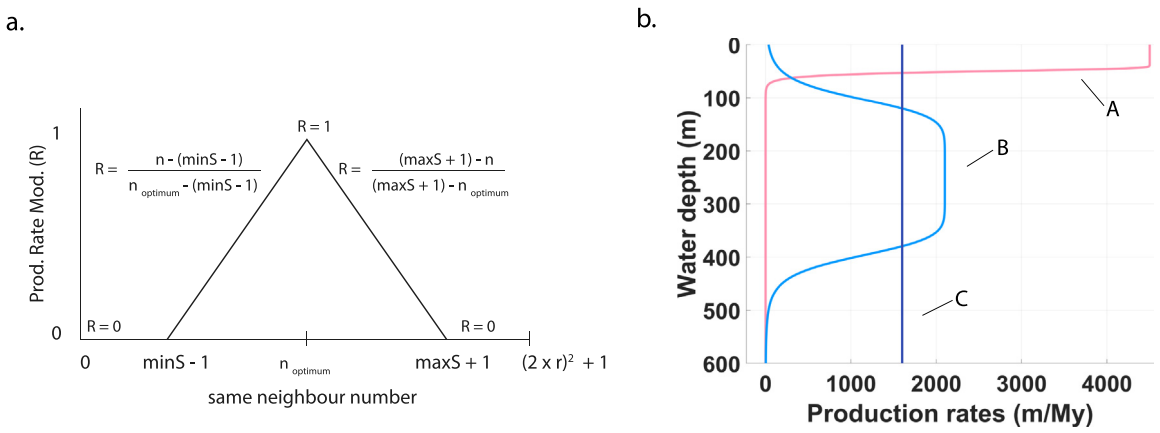

Fig. 4. a. Production rate modifier (R) rationale in CarboCAT. R is equal to 1 (maximum carbonate production) in model cells with the optimum amount of same-facies neighbours ($n_{optimum}$), corresponding to the midrange of the minimum and maximum survival values ($minS$ and $maxS$, see Fig. 3). R decreases linearly from 1 to zero where the number of same-facies cells is equal to $minS$ or $maxS$ and the resulting carbonate production is zero. b. depth-dependent production profiles representing different factories: euphotic production profile (A), oligophotic production profile (B) and aphotic production profile (C).

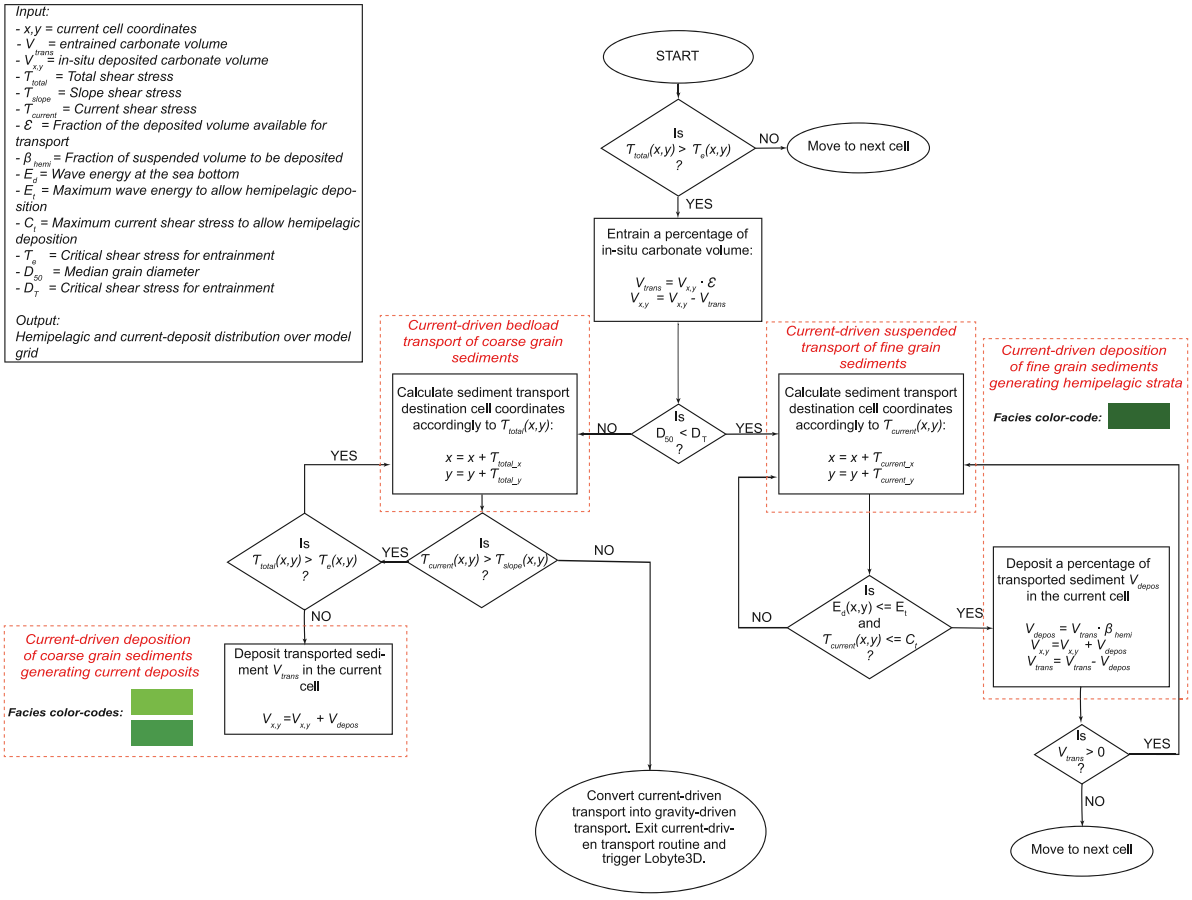

Fig. 5. Flow chart describing the current-driven suspended and bedload transport algorithm operation for any model grid cell.

1.4.1. Carbonate sediment entrainment

Entrainment of carbonate sediment is calculated assuming entrainment occurs when total shear stress acting on grains is greater than the critical shear stress for entrainment (Warrlich et al., 2002).

Total shear stress is the combination of the shear stress generated by currents ($\tau_{current}$), and the shear stress generated by the slope (τ_{slope}), which is directly related to the gravity forces acting on the carbonate grains:

$$\tau_{total} = \tau_{current} + \tau_{slope} \quad (1.4.1)$$

Following Warrlich et al. (2002)., slope shear stress is calculated as:

$$\tau_{slope} = \delta_\rho g D_{50} G \quad (1.4.2)$$

where, δ_ρ is the difference between water and sediment density, and G is the magnitude of the topographic gradient vector.

Current shear stress magnitude and direction is controlled by the user either selecting a single value, assigned to every model x, y cell, representing a constant, unidirectional current across the entire model

grid, or a distinct value for every grid cell, representing more complex scenarios, for example diverging fluid flow occurring around and over an isolated platform due to thermohaline circulation flow. Maximum current magnitude occurs at the water surface, and decreases exponentially with water depth.

Critical entrainment shear stress is a function of the sediment grain size and angle of repose, using equation (20) of Warrlich et al. (2002):

$$\tau_e = \delta_\rho g D_{50} \sin \alpha_c \tag{1.4.3}$$

where α_c is the angle of repose. Sediment entrainment occurs when total shear stress at the sediment–water interface, τ_{total}, exceeds critical shear stress for entrainment for the grain size produced in that cell for that iteration.

The volume of sediment that is removed from each x, y cell where entrainment conditions are met ($T_{out\ x,y}$), is calculated as:

$$T_{out\ x,y} = E_{x,y} \cdot t_f \tag{1.4.4}$$

where t_f is the *fraction index*, a parameter selected by the user for each modelled facies accordingly to the facies erodibility. For example, a high-mobility ooidal sand should have a higher *fraction index* (e.g. $t_f = 0.9$) than a coral framestone (e.g. $t_f = 0.4$) characterized by a rigid framework.

In the current CarboCAT version, nor model substratum or pelagic sediments can be eroded and transported.

1.4.2. Current-driven sediment transport and deposition

Once a volume of sediment has been entrained, transport across the platform follows different mechanisms, depending whether particles are being carried in suspension or as bed load.

Transport direction of suspended particles is controlled by the 2D current vector field alone. Sediments are moved from the entrainment point up to the first cell where the current shear stress is zero, indicative of deep water conditions where low energy allows fine grain particle to settle, either a local intra-platform lagoon or the main oceanic basin. When the latter condition is met, a percentage of suspended volume is deposited, but the rest of the sediment remains in suspension and moves into the next cell along the current vector, where the above criteria are retested. Transport and deposition continues along the current vector until all suspended sediment volume is deposited, or until a model boundary is reached and the sediment exits the model.

Sediment transport by bed load is controlled by both unidirectional current shear stress, and gravity forces related to sea-floor gradient. When current shear stress is higher than slope shear stress, transport is current-driven and the sediment pathway is controlled by the total shear stress vector field, τ_{total}. Deposition of current-driven bedload occurs when total shear stress in a grid cell drops below the critical shear stress for entrainment. At this point, all entrained sediment volume is deposited and, if there is not enough accommodation, excess sediment is redistributed equally across adjacent cells.

Current-driven transport by bedload is converted into gravity-driven transport when the slope shear stress exceeds the current shear stress, for example when sediment being transported across the shallow-water platform, reaches the steep gravity-dominated platform slope.

1.4.3. Gravity-driven sediment transport and deposition

Gravity-driven carbonate resedimentation plays a critical role in development of carbonate systems (e.g. Williams et al., 2011; Pomar and Hallock, 2008; Schlager, 2005; Pomar, 2001; Aurell et al., 1995). Turbidity currents and debris flows funnel grainy platform-top sediments basinward, generating slope deposits and basin-floor fans and aprons. On the shallow platform top, small-scale gravity-driven transport locally reworks in-situ carbonates, generating resedimented strata that increase platform heterogeneity.

In CarboCAT, the Lobyte3D algorithms (Burgess et al., 2019) calculate gravity-driven sediment transport and deposition. When entrained sediment moves onto or a volume of sediment is entrained on a steep area of the platform, Lobyte3D transports the sediment down slope following the steepest route from cell to cell, simulating a laterally-confined flow. Flow velocity is calculated as a function of topographic gradient and flow thickness is increased by the run-up height, h_r, defined by Kneller and Buckee (2000) as the maximum height that can be reached by a flow for a given velocity and calculated by

$$h_r = \frac{U^2}{2 \cdot g} \tag{1.4.5}$$

where g is acceleration due to gravity and U is the flow velocity.

When the flow reaches a point where slope drops below a threshold value required to maintain sufficient velocity, the flow front becomes dispersive and, bathymetry permitting, sediments are progressively deposited, to generate a typically lobate deposit. Starting from the cell occupied by the whole flow volume and assuming that flow concentrates in the direction of maximum slope, the proportion, ΔV_k, of sediment volume $V_{i,j}$ received by each surrounding cell is proportional to the gradient from the source cell G_k, so

$$\Delta V_k = \left[G_k^{FRF} \cdot \left(\sum_{k=1}^{8} G_k \right)^{-1} \right] \cdot V_{i,j} \qquad where \quad k = 1, 2, 3, \ldots, 8; \tag{1.4.6}$$

modified from Trauth (2015), where the flow radiation factor FRF controls the degree of flow dispersion. Sediment thickness deposited in each cell reached by the dispersive flow is calculated as a given proportion of sediment volume $V_{i,j}$ that flowed into the cell.

1.5. Siliciclastic sediment input

Terrigenous sediment input to carbonate producing areas can be an important control on carbonate platform architecture and facies heterogeneity. Suspended siliciclastic sediments inhibit, or even end, carbonate production across the platform by decreasing water column light levels (e.g. Hallock et al., 1986) or even burying organisms. Siliciclastic input may also increase heterogeneity by producing siliciclastic beds within carbonate strata.

CarboCAT implements two distinct mechanisms for modelling siliciclastic input and deposition. In both modes, sediments are sourced from either linear or point sources on the model grid boundary, and then transported and deposited within the model. Transport and deposition is calculated using either the Lobyte3D algorithm described in Section 1.4.3 to represent event-based transport and deposition influenced by basin-floor topography, or a diffusion-based algorithm, simulating topography-independent dispersion of a suspended sediment plume where sediment concentration decreases from the sediment source due to dispersion and hemipelagic deposition.

Siliciclastic diffusion is governed by Fick's second law (Crank, 1979), expressing the change of sediment concentration in the water column δC in the x and y directions in function of time t:

$$\frac{\delta C}{\delta t} = D_x \frac{\delta^2 C}{\delta x^2} + D_y \frac{\delta^2 C}{\delta y^2} \tag{1.5.1}$$

where D_x and D_y are the diffusion coefficient in the x and y directions, respectively. These diffusion coefficients are defined by the user and, in the current version of CarboCAT, they are not affected by currents and waves.

1.5.1. Carbonate production inhibition

CarboCAT calculates carbonate accumulation in every grid cell x, y where simultaneous siliciclastic deposition occurs, by computing a new water depth production profile that use a value of the saturation light intensity, I_s, proportional to the siliciclastic concentration in the same cell $C(x, y)$ as follows:

$$I_s = I / (1 - \frac{C(x, y)}{C_f}) \tag{1.5.2}$$

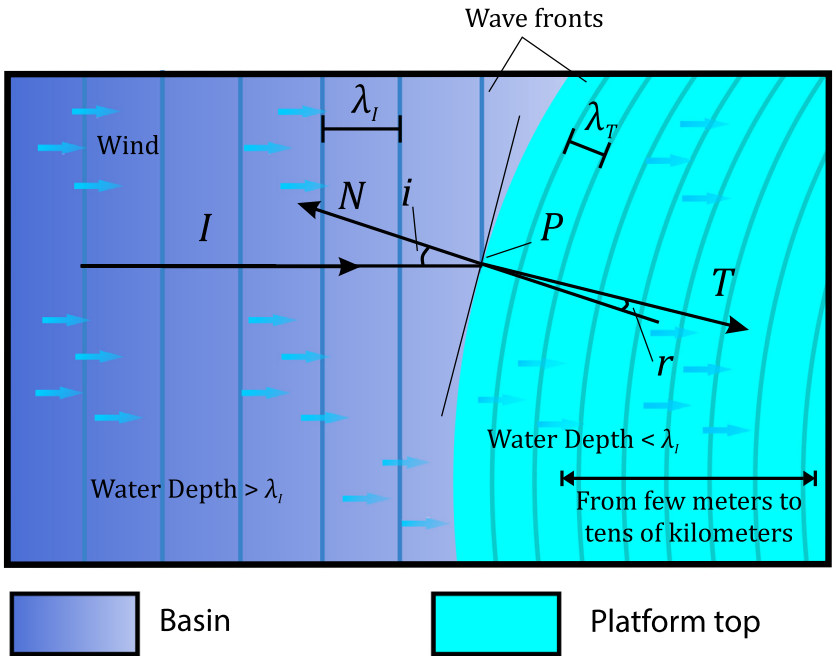

Fig. 6. Ray tracing in map view. Wave refraction occurs when the incidence wave ray I approaches a shallow water area with an angle i; the transmitted wave ray T bends and propagates with a lower velocity due to bottom friction.

where, C_f is the siliciclastic concentration required to completely kill the production of the factory f. C_f is defined for each produced carbonate facies, allowing simulation of carbonate facies with different sensitivities to siliciclastic poisoning.

1.6. Wave energy

Another new addition to CarboCAT is an algorithm to model wind-generated wave propagation and resulting wave energy distribution over the carbonate platform area. Wave paths are calculated with a 2D ray-tracing method (e.g Johnson and Morrough, 1948; Arthur et al., 1952), wave parameters are estimated using linear wave theory equations, and the resulting wave energy spatial distribution controls location of any carbonate factories defined to be sensitive to wave energy conditions.

The unit vector W describes wind propagation over the model area. This wind vector field is assumed to be unidirectional and has constant velocity at each model grid point. Wind velocity determines the amplitude of generated waves and consequently controls wave energy and wave penetration into shallow water areas. High-amplitude waves carry more energy but their greater wave-break depth prevents propagation into the shallowest water areas of the platform top.

Wave rays are traced from each cell of the windward model boundary where they are initiated. Initial propagation direction is controlled by wind direction. Wave refraction may then occur at the boundary between two cells, when the traced ray approaches a relatively shallow water area and water depth is less than half of the wave wavelength (Fig. 6). Propagation terminates when the wave path encounters a shallow-water area where the wave breaks, or when it reaches one of the model boundaries, leaving the model grid. The angle of refraction r of each wave is determined by Snell's Law:

$$r = \sin^{-1}\left(\frac{\lambda_T}{\lambda_I}\sin i\right) \tag{1.6.1}$$

where the incidence angle i is defined as the angle between the vector of the arriving wave and the unit normal vector to the local bathymetry, which is the gradient of the bathymetry in the cell where refraction occurs; λ_T and λ_I are the wavelength of the transmitted and incidence rays, respectively. The wavelength of the propagating wave, in areas where the water depth is more than half the ray wavelength, is calculated using the following equation:

$$\lambda_{shallow} = \lambda_{deep}\left\{\tanh\left[\left(\frac{2\pi\sqrt{\frac{d_{yx}}{g}}}{T}\right)^{\frac{3}{2}}\right]^{\frac{2}{3}}\right\} \tag{1.6.2}$$

where, g is the gravitational constant in m/s^2, T is the wave period in s and d_{xy} is the water depth in meters. Eq. (1.6.2) was proposed by Fenton and McKee (1990) and already implemented by Mandlier and Kench (2012) in an analytical model of wave refraction. The wavelength of the propagating wave, in areas where the water depth is less than half the ray wavelength, is calculated using the Airy wave theory equation:

$$\lambda_{deep} = \frac{gT^2}{2\pi} \tag{1.6.3}$$

The energy density E_0 carried by each propagating wave is measured in Joule per square meter and calculated according to Airy's theory as follow:

$$E_0 = \frac{\rho g h_w^2}{8} \tag{1.6.4}$$

Where, ρ is the water density and the value of the wave height h_w is calculated using the following equation:

$$h_w = 0.283\tanh\left[0.0125\left(\frac{gF}{U_{wind}^2}\right)^{0.42}\right]\frac{U_{wind}^2}{g} \tag{1.6.5}$$

where U_{wind} is the wind velocity, and F is the fetch area in square meters that increases with wave propagation distance. In areas where water depth is less than half the wavelength, wave propagation is affected by sea floor bottom friction, and all or part of the wave energy is dissipated. Energy dissipation is calculated using equation (9) of Terray et al. (1996):

$$\epsilon = \frac{\left(0.3\frac{d_{xy}}{h_w}\right)^{-2}}{\left(0.3\frac{h_w/0.78}{h_w}\right)^{-2}} \tag{1.6.6}$$

Table 1
General and structural parameters with specified literature sources, used in the four model runs.

Parameters	Values	Reasonable and references
Run time	3 My	Reasonable observation period, allowing the modelled faults to develop significant displacement.
Time step	1000 yr	Trade-off between model resolution and run time.
Cell size	200 m	Trade-off between model resolution and run time.
Model area	16 x 16.2 km^2	Reasonable scale for the represented structural scenarios.
Structural parameters		
Regional subsidence	180 m My^{-1}	Allen and Allen (e.g. 2013)
Slip rate	0.4 mm y^{-1} *(H)*; 0.6 mm y^{-1} *(HG)*	Realistic values for extensional faults. Slip rates measured over different time intervals can be found in Mouslopoulou et al. (2009).
Fault dip	90°	Value recommended in Carbo-CAT to avoid artefacts when faults have horizontal displacements exceeding cell size.
Final fault length	20 km *(H)*; 25 km *(HG)*	Fault length is calculated using the displacement/length relationship proposed by Cowie and Scholz (1992).
Foot-wall uplift	0.10 km *(H)*; 0.15 km *(HG)*	Foot-wall uplift is generally between 5%–10% of the total hanging-wall subsidence (e.g. Jackson and McKenzie, 1988).
Hanging-wall subsidence	1 km *(H)*; 1.5 km *(HG)*	Consistent with the desired slip rate.

Maximum wave energy at the sea surface becomes:

$$E_0 = E_0(1 - \epsilon) \tag{1.6.7}$$

To calculate the sea-floor wave energy, decreasing with increasing water depth as radius of wave orbital motion decreases, a simple exponential function is used:

$$E_d = E_0 \left[\tanh\left(e^{-kd}\right)\right] \tag{1.6.8}$$

where k is a user defined exponential factor and d is the water depth in meters. Waves break and dissipate all their energy when water depth is less than the break depth of the wave $0.78h_w$. After breaking occurs, the width of the surf zone over which wave energy is dissipated is currently defined as a CarboCAT input parameter rather than calculated. A more complex algorithm, modelling the effect of waves on sediment redistribution and currents is currently under development.

1.7. Post-processing and graphical output

CarboCAT includes various post-processing code modules to calculate volumes of facies, generate geobody distributions, calculate timeseries of strata properties, and test for order in the modelled stratigraphy (Burgess, 2016a,b). CarboCAT also includes code to generate 3D graphical output, as well as 2D cross-sections and chronostratigraphic diagrams and map views of all the modelled strata. To facilitate use of CarboCAT to study subsurface datasets, we also use depth-domain 3D-convolution seismic modelling, integrating both illumination and resolution effects (Lecomte et al., 2015; Lecomte, 2008), to develop synthetic seismic images from Carbo-CAT facies models. Most generated seismic images include layered overburden strata composed of alternating shale and sand strata. The effect of diagenetic transformations and differential compaction can strongly affect the seismic appearance of carbonate strata (e.g. Fournier et al., 2014). These processes are currently not modelled in CarboCAT, however, future developments and applications will explore these limitations.

2. CarboCAT applications

To demonstrate that CarboCAT can usefully model carbonate strata, two example model runs generate carbonate platform geometries typical of extensional tectonic settings. One is an isolated platform on a horst and the other is a land-attached platform on a half-graben. We qualitatively compare these numerical stratigraphic models and the resulting synthetic seismic with previous general conceptual models (e.g Bosence, 2012; Williams et al., 2011; Dorobek, 2011; Cross and Bosence, 2008; Wilson et al., 2000; Leeder and Gawthorpe, 1987). These conceptual models provide detailed description of platform architecture and facies distribution developed in response to syn-tectonic structural evolution of the tectonic basement. If CarboCAT can reproduce these conceptual models then that is evidence that the processes implemented in our numerical model are sufficiently realistic to be useful. Conversely, if our numerical model results show significant differences, or require unrealistic parameters to match the conceptual models, this may indicates a problem with one or the other that requires further investigation.

Also, to demonstrate that CarboCAT can be a useful tool for experimental forward modelling to explore how carbonate platforms may evolve, we use CarboCAT to characterize in-situ-dominated versus transport-dominated syn-tectonic platforms. Two additional models demonstrate how increase in sediment transport rates is alone sufficient to generate a different platform-type, with different stratal geometries.

2.1. Input parameters

Input parameters used in our simulations are listed in Tables 1–4. These parameters were derived from various literature sources to be consistent with the modelled geological scenarios; further informations are provided below.

Initial bathymetry - Carbonate production initiation requires, among other things, for the depositional surface to be at least partially submerged. Since in most extensional settings this occurs after some degree of extension has already taken place (e.g. Suez Rift; Gawthorpe and Leeder, 2000), initial bathymetry for our model runs represents an early extensional stage (Fig. 7a–b).

Sea-level curve - To evaluate stratigraphic hiatuses, the sea-level curve used in our model simulations has a 120 m amplitude and a relatively high-frequency asymmetric cycle (Fig. 7c), modelling the effect of slow ice sheet growth and subsequent rapid melting during an overall ice-house climate internal (e.g. Goldhammer et al., 1987).

Carbonate factories - Carbonate factory input parameters are listed in Table 2. In-situ carbonate factory production rates are constrained by present-day observations of reef margin and platform interior facies (e.g. Schlager, 2000; Bosence et al., 1994). The magnitude of the minimum and maximum values for the wave energy, required by the in-situ facies to survive, is consistent with measurements of wind wave energy across a reef fringed platform area (e.g. Péquignet et al., 2011). Two fractions of in-situ sediment available for transport have been listed for each factory; a low to medium transport rate regime is modelled with a transportable sediment proportion of $0.4 - 0.85$, and a high-transport rate system with a $0.9 - 0.95$ proportion.

Siliciclastic input - During lowstands, land-attached carbonate platform systems may be affected by siliciclastic sediment deposition generated by the base level lowering, encouraging erosion on the mainland (Davies et al., 1989). To simulate this event, a variable (Fig. 7d) volume of siliciclastic sediment is introduced in the half-graben model runs during sea-level low; location of the sediment input point is shown in Fig. 7(a).

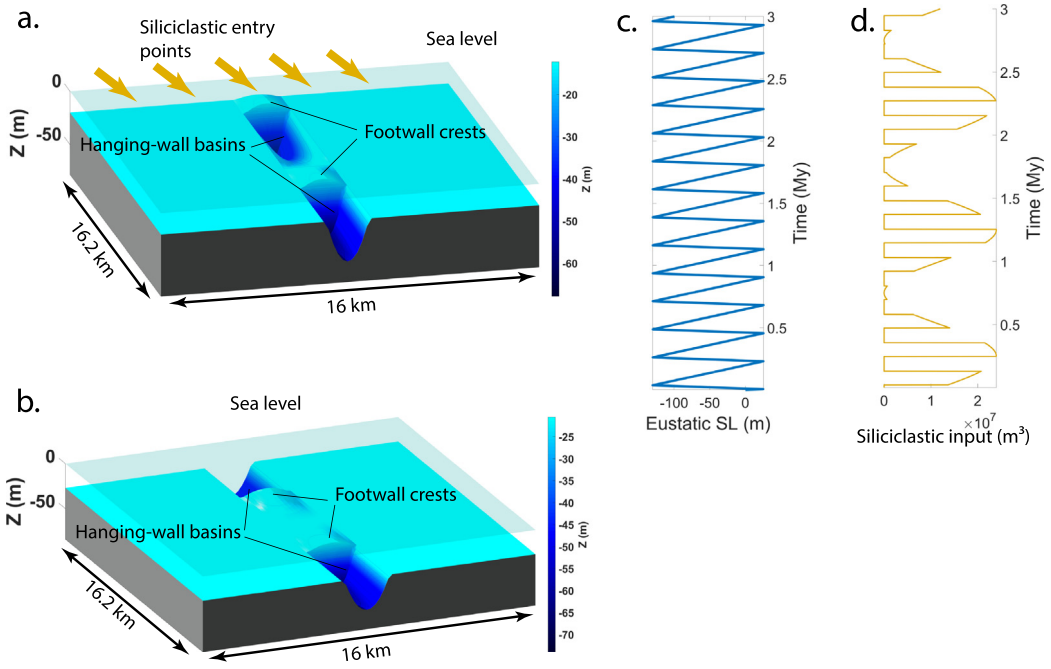

Fig. 7. CarboCAT input parameters. Initial bathymetry for a. half graben model run and b. horst model run; c. eustatic sea level curve used in all model runs; d. siliciclastic input variable volume curve used in Model run 2 and 2b, note that siliciclastic sediments are introduced in the model only during low stands.

Table 2
Carbonate factories input parameters. Two fractions of in-situ sediment available for transport have been listed for each factory: a low to medium transport rate regime (Model run 1 and 2; fraction index, t_f, equal to 0.4 – 0.85) and a high-transport rate system with t_f equal to 0.9 – 0.95 (Model run 1b and 2b).

Factory	Production rate (max)	Wave energy	Median grain diameter	Fraction index (t_f)
Reef	4500 m My^{-1}	> 4 · 10^4 J m^{-2}	0.5 mm	0.4 (Model Runs 1, 2) – 0.9 (Model Runs 1b, 2b)
Interior 1	2500 m My^{-1}	< 4 · 10^4 J m^{-2}	0.1 mm	0.85 (Model Runs 1, 2) – 0.95 (Model Runs 1b, 2b)
Interior 2	2500 m My^{-1}	< 4 · 10^4 J m^{-2}	0.05 mm	0.85 (Model Runs 1, 2) – 0.95 (Model Runs 1b, 2b)
Pelagic	80 m My^{-1}	= 0· J m^{-2}	–	–

Table 3
Wave energy, currents and sediment transport parameters.

Environmental parameters	Values	Reasonable and reference
Wind velocity	18 m s^{-1}	Beaufort scale (near-gale).
Wave period in deep water	8 s	Observed ocean wave periods lie between 3 and 20 s (e.g. Mandlier and Kench, 2012; Péquignet et al., 2011).
Wave base	−80 m	
Fetch length outside model boundary	4 km	Distance from the subsequent structural high.
Grain size threshold between suspended/bedload transport	0.09 mm	Determined in agreement with the grain size of the modelled factories such as one of them generates hemipelagic sediments.
Lower boundary for wave induce current	−80 m	In agreement with the wave base boundary.

Acoustic properties - Acoustic properties used to populate the geological model and develop the synthetic seismic are listed in Table 4, and chosen between various literature sources (e.g. Fournier et al., 2014; Anselmetti and Eberli, 1993) in agreement with the modelled facies, to generate acoustic impedance contrasts between the various rock types.

Table 4
Acoustic properties.

Rock type/Facies	Density (g cm^{-3})	P-wave velocity (m s^{-1})
Reef and derived current deposit	2.53	4688
Interior 1 and derived current deposit	2.74	5996
Interior 2 and derived hemipelagic	2.78	6000
Gravity flow deposits	2.67	5259
Siliciclastic	2.4	3000
Pelagic	2.8	6283
Basement	2.9	5500

2.2. Model run 1: isolated horst

The tectono-stratigraphic conceptual model of horst carbonate platform proposed by Dorobek (2011) is summarized in Fig. 8(a), and the equivalent CarboCAT modelling results presented in Fig. 8(b–h).

Comparison with observations - The CarboCAT isolated horst model shows displacement accumulated over symmetric bounding faults, resulting in the development of an uplifted structure flanked by hanging-wall basins (Fig. 8(b)). Symmetric footwall crests uplift folds carbonate strata into gentle synclines and generates apparent 'sagging' of inner platform strata (Fig. 8(e,g)), in agreement with Dorobek (2011) conceptual models. Windward–leeward facies variability is also represented, with high-stand shedding (Schlager et al., 1994) of fine-grained sediments into the leeward basin (Fig. 8(c)) and preferential reef growth on the windward footwall crest (Fig. 8(b)). Sea-level oscillations generate subaerial exposure surfaces on platform top; the longest hiatuses occur on the highest-relief windward footwall crest (Fig. 8(c)).

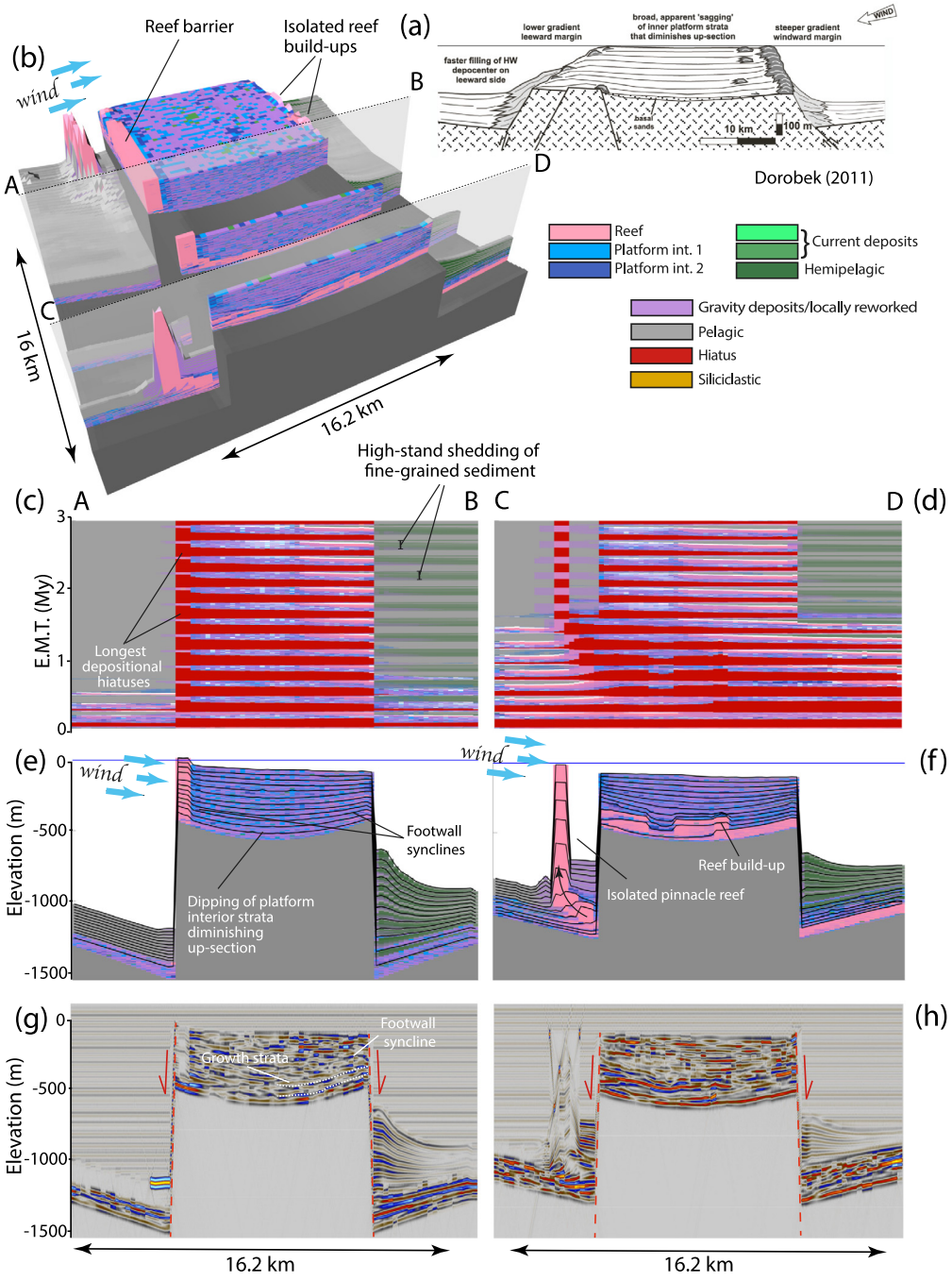

Fig. 8. (a–h) Comparison between the generalized tectono-stratigraphic model proposed by Dorobek (2011) and Model run 1 results; (a) Tectono-stratigraphic conceptual model of a horst carbonate platform (modified from Dorobek, 2011); (b) CarboCAT 3D facies model; (c–d) Chrono-stratigraphic diagrams; (e–f) Cross-sections; (g–h) Synthetic seismic sections generated using a 30 Hz Ricker wavelet. Note the development of isolated pinnacle reefs on the hanging-wall basin showing a curved stacking pattern generated by progradation followed by aggradation during hanging-wall rotation.

2.3. Model run 2: half-graben

The tectono-stratigraphic conceptual model of carbonate platform development on half-graben proposed by Dorobek (2011) is summarized in Fig. 9(a), and the equivalent CarboCAT modelling results presented in Fig. 9(b–h).

Comparison with observations - The CarboCAT half-graben model includes two parallel faults with the same dip direction, driving fault block rotation (Fig. 9(b)) and generating characteristic stratal patterns described by authors (e.g Dorobek, 2011; Cross and Bosence, 2008; Leeder and Gawthorpe, 1987) and adequately replicated in our CarboCAT model. These geometries include basinward diverging strata (Fig. 9(e)) and upward flattening of carbonate strata that were initially parallel to the foot-wall dip slope (Fig. 9(g)). Reefal facies develop on the windward footwall crest (Fig. 9(b)) and, away from the fault depocentre, on the hanging-wall margin (Fig. 9(f)). These strata backstep towards the footwall crest under the effect of fault block rotation and dip-slope water deepening. Windward basin stratigraphy is relatively thin, while the more proximal graben contains significant thickness of siliciclastic strata transported into the basin across several glacio-eustatic sea-level cycles, but forming longer-term alternations with pelagic carbonates due to variable input volume (Fig. 9(c,e)).

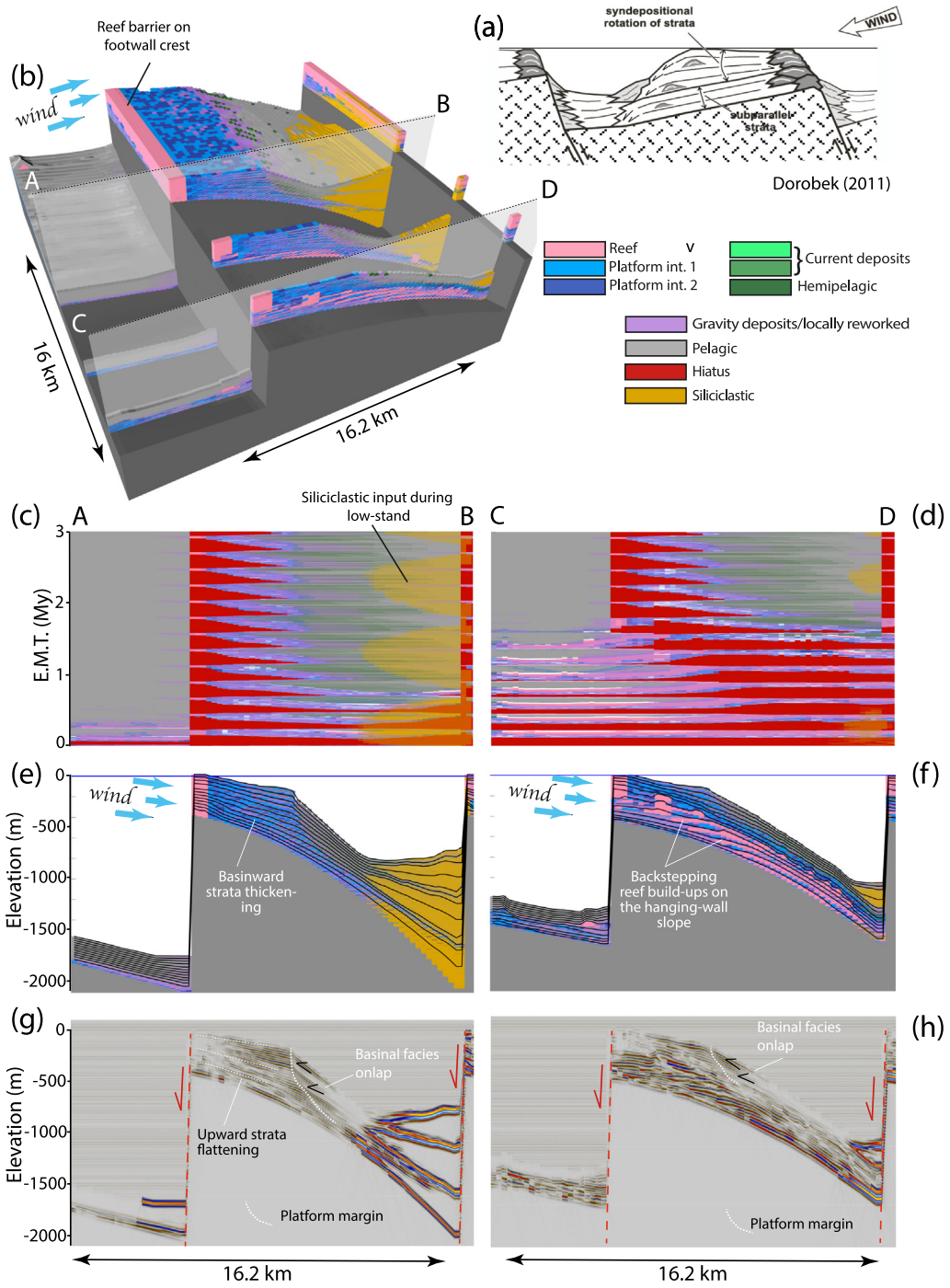

Fig. 9. (a–h) Comparison between the generalized tectono-stratigraphic models proposed by Dorobek (2011) and Model run 2 results; (a) Tectono-stratigraphic conceptual model of a half-graben carbonate platform (modified from Dorobek, 2011); (b) CarboCAT 3D facies model; (c–d) Chrono-stratigraphic diagrams; (e–f) Cross-sections; (g–h) Synthetic seismic sections generated using a 30 Hz Ricker wavelet.

2.3.1. Model run 1b and 2b: isolated horst and half-graben with high transport rates

The importance of sediment transport as a control on carbonate platform geometry is now well understood (e.g. Williams et al., 2011; Pomar and Hallock, 2008; Schlager, 2005; Pomar, 2001; Aurell et al., 1995). In Model run 1b and 2b the *fraction index*, t_f, has been increased (see Table 2) to simulate carbonate platform development in under high erosion rates. Higher rates of sediment transport reduce platform accumulation and increase basin re-sedimentation, generating transport-dominated ramp platforms (Fig. 10(g)) rather than the in-situ dominated platforms produced in Model runs 1 and 2. Platform margin relief and water depth asymmetry is subdued by resedimentation into adjacent grabens (e.g. Fig. 10(c)). Horizontal and vertical facies heterogeneity is increased throughout due to mixing of in-situ and transported layers (e.g. Fig. 10 (c,d)).

3. Conclusions

The new version of CarboCAT includes simplified, but physically reasonable representations of the complex processes influencing carbonate strata development in tectonically active settings.

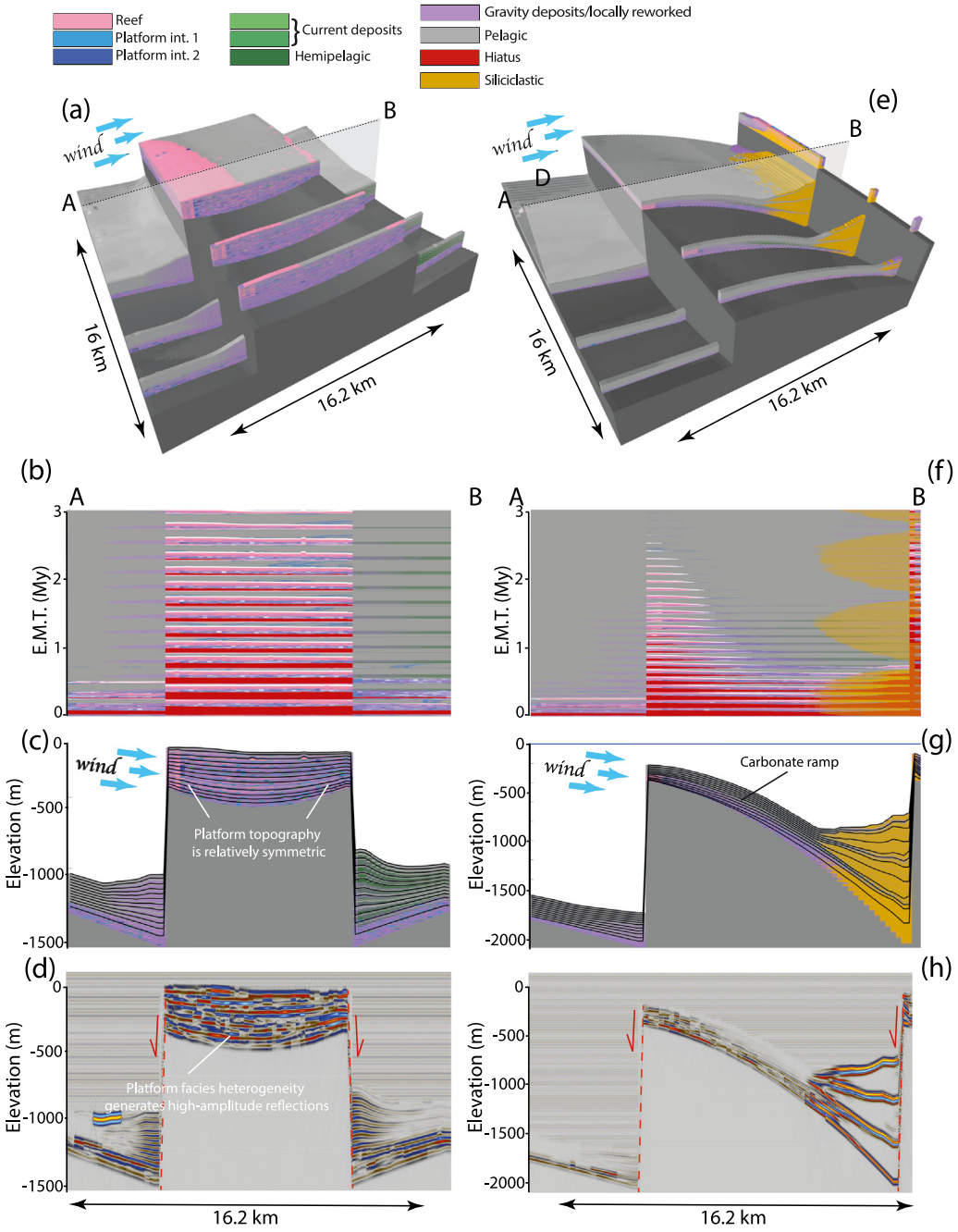

Fig. 10. (a–d) modelling results of Model run 1b, simulating transport-dominated platform on horst; (e–h) modelling results of Model run 2b, representing transport-dominated platform on half-graben.

Model runs of carbonate strata deposited in horst and half-graben settings successfully reproduce platform morphologies and facies distributions described in conceptual models (e.g Bosence, 2012; Williams et al., 2011; Dorobek, 2011; Cross and Bosence, 2008; Wilson et al., 2000; Leeder and Gawthorpe, 1987) suggesting the new model formulation and the input parameter values used are all reasonable.

Comparison of in-situ dominated platform geometries with transport-dominated equivalents shows how a combination of experimental and constrained best-fit modelling approaches can help significantly enhance our understanding of carbonate strata and carbonate platforms.

Computer code availability

CarboCAT version described here is written in MATLAB (R2018a) and available for downloading, alongside with a tutorial, from the following git repository: https://github.com/Isabelle16/CarboCAT2018a.

Declaration of competing interest

The authors declare that they have no known competing financial interests or personal relationships that could have appeared to influence the work reported in this paper.

Acknowledgements

Masiero would like to acknowledge financial support from Tullow Oil, Woodside Petroleum, and Wintershall. Antonatos would like to acknowledge financial support from BP. Kozlowski would like to acknowledge financial support from Baker Hughes and BP. The authors thank NORSAR Innovation AS for the academic use of SeisRoX to create synthetic seismic images, and Schlumberger for use of Petrel software for aspects of 3D model visualisation. Georg Warrlich and an anonymous reviewer provided many constructive comments on the original manuscript that were very useful helping us better explain and focus our arguments.

References

Allen, P.A., Allen, J.R., 2013. Basin analysis: Principles and Application to Petroleum Play Assessment. John Wiley & Sons, p. 549.

Anselmetti, F.S., Eberli, G.P., 1993. Controls on sonic velocity in carbonates. Pure Appl. Geophys. 141 (2–4), 287–323. http://dx.doi.org/10.1007/BF00998333.

Antonatos, G., 2018. Effect of Carbonate Platform Controls on Large Scale Platform Heterogeneity and Seismically Imaged Geometries (Ph.d. dissertation). Royal Holloway, University of London, London, p. 404.

Arthur, R.S., Walter, H.M., John, D.I., 1952. The direct construction of wave rays. EOS Trans. Am. Geophys. Union 33 (6), 855–865.

Aschoff, J., Rountree, J., 2012. Evaluating the roles of sediment supply and tectonics using growth-strata analysis , sequence stratigraphy , forward stratigraphic modeling and sediment volume Calculations : An example from the cordilleran foreland C.

Aurell, M., Bosence, D., Waltham, D., 1995. CaRbonate ramp depositional systems from a late jurassic epeiric platform (iberian basin, Spain): a combined computer modelling and outcrop analysis. Sedimentology 42 (1), 75–94. http://dx.doi.org/10.1111/j.1365-3091.1995.tb01272.x.

Bosence, D., 2012. CaRbonate-dominated marine rifts. In: Regional Geology and Tectonics: Phanerozoic Rift Systems and Sedimentary Basins. Elsevier B.V., pp. 104–130. http://dx.doi.org/10.1016/B978-0-444-56356-9.00005-5.

Bosence, D.W., Pomar, L., Waltham, D.A., Lankester, T.H., 1994. Computer modeling a miocene carbonate platform, mallorca, Spain. Amer. Assoc. Pet. Geol. Bull. 78 (2), 247–266.

Bosence, D., Waltham, D., 1990. Computer modeling the internal architecture of carbonate platforms. Geology 18 (1), 26–30. http://dx.doi.org/10.1130/0091-7613(1990)018<0026:CMTIAO>2.3.CO;2.

Bosscher, H., Schlager, W., 1992. Computer simulation of reef growth. Sedimentology 39 (3), 503–512. http://dx.doi.org/10.1111/j.1365-3091.1992.tb02130.x.

Brasington, J., Richards, K., 2007. Reduced-complexity, physically-based geomorphological modelling for catchment and river management. Geomorphology 90 (3–4), 171–177. http://dx.doi.org/10.1016/j.geomorph.2006.10.028.

Burgess, P.M., 2006. The signal and the noise: Forward modeling of allocyclic and autocyclic processes influencing peritidal Carbonate stacking patterns. J. Sediment. Res. 76 (7), 962–977. http://dx.doi.org/10.2110/jsr.2006.084.

Burgess, P.M., 2012. A brief review of developments in stratigraphic forward modelling, 2000-2009. In: Regional Geology and Tectonics: Principles of Geologic Analysis, Vol. 1. pp. 379–404. http://dx.doi.org/10.1016/B978-0-444-53042-4.00014-5.

Burgess, P.M., 2013. CaRbocat: A cellular automata model of heterogeneous carbonate strata. Comput. Geosci. 53, 129–140. http://dx.doi.org/10.1016/j.cageo.2011.08.026.

Burgess, P.M., 2016a. Identifying ideal stratigraphic cycles using a quantitative optimization method. Geology 44 (6), 443–446. http://dx.doi.org/10.1130/G37827.1.

Burgess, P.M., 2016b. Identifying ordered strata: Evidence, methods, and meaning. J. Sediment. Res. 86 (3), 148–167. http://dx.doi.org/10.2110/jsr.2016.10.

Burgess, P.M., Masiero, I., Toby, S.C., Duller, R.A., 2019. A big fan of signals? exploring autogenic and allogenic process and product in a numerical stratigraphic forward model of submarine-fan development. J. Sediment. Res. 89 (1), 1–12. http://dx.doi.org/10.2110/jsr.2019.3.

Burgess, P.M., Wright, V.P., Emery, D., 2001. Numerical forward modelling of peritidal carbonate parasequence development: Implications for outcrop interpretation. Basin Res. 13 (1), 1–16. http://dx.doi.org/10.1046/j.1365-2117.2001.00130.x.

Clarke, K.C., Gaydos, L., Hoppen, S., 1997. A self-modifying cellular automaton model of historical urbanization in the san francisco bay area. Environ. Plann. B: Plann. Des. 24, 247–261.

Cowie, P.A., Scholz, C.H., 1992. Displacement-length scaling relationship for faults: data synthesis and discussion. J. Struct. Geol. 14 (10), 1149–1156. http://dx.doi.org/10.1016/0191-8141(92)90066-6.

Crank, J., 1979. The Mathematics of Diffusion. Oxford university press, p. 414.

Cross, N.E., Bosence, D.W.J., 2008. Tectono-sedimentary models for rift-basin Carbonate systems. Controls Carbonate Platf. Reef Dev. 83–105. http://dx.doi.org/10.2110/pec.08.89.0083.

Csato, I., Kendall, C.G.C., 2002. Modeling of stratigraphic architectural patterns in extensional settings - towards a conceptual model. Comput. Geosci. 28 (3), 351–356. http://dx.doi.org/10.1016/S0098-3004(01)00056-5.

Davies, P.J., Symonds, P.A., Feary, D.A., Pigram, C.J., 1989. The evolution of the carbonate platforms of northeast Australia.. Controls Carbonate Platf. Basin Dev. 44, 233–258.

Dorobek, S.L., 2011. Tectonic and depositional controls on syn-rift Carbonate platform sedimentation. Controls Carbonate Platf. Reef Dev. 57–81. http://dx.doi.org/10.2110/pec.08.89.0057.

Fenton, J.D., McKee, W.D., 1990. On calculating the lengths of water waves. Coast. Eng. 14 (6), 499–513.

Flake, G.W., 1998. The Computational Beauty of Nature: Computer Explorations of Fractals, Chaos, Complex Systems, and Adaptation. MIT press, p. 401.

Fournier, F., Léonide, P., Kleipool, L., Toullec, R., Reijmer, J.J., Borgomano, J., Klootwijk, T., Van Der Molen, J., 2014. Pore space evolution and elastic properties of platform carbonates (urgonian limestone, barremian-aptian, SE France). Sediment. Geol. 308, 1–17. http://dx.doi.org/10.1016/j.sedgeo.2014.04.008.

Gawthorpe, R., Leeder, M., 2000. Tectono-sedimentary evolution of active extensional basins. Basin Res. 12 (3–4), 195–218. http://dx.doi.org/10.1111/j.1365-2117.2000.00121.x.

Goldhammer, R.K., Dunn, P.A., Hardie, L.A., 1987. High frequency glacio-eustatic sealevel oscillations with milankovitch characteristics recorded in middle triassic platform carbonates in northern Italy. Amer. J. Sci. 287, 853–892.

Griffiths, C., Dyt, C., Paraschivoiu, E., Liu, K., 2001. Sedsim in hydrocarbon exploration. In: Merriam, D., Davis, J.C. (Eds.), Geologic Modeling and Simulation. Kluwer Academic, New York, pp. 71–97. http://dx.doi.org/10.1007/978-1-4615-1359-9, URL http://link.springer.com/10.1007/978-1-4615-1359-9.

Haiwei, X., in prep., Ph.d. dissertation. University of Liverpool, Liverpool.

Hallock, P., Schlager, W., Hallock, P., 1986. Nutrient excess and the demise of coral reefs and Carbonate platformns. Palaios 1 (4), 389–398.

Jackson, J., McKenzie, D., 1988. Rates of active deformation in the Aegean Sea and surrounding regions. Basin Res. 1 (3), 121–128.

Johnson, J.W., Morrough, P.O., 1948. Graphical Construction of Wave Refraction Diagrams. United States Navy Department, Hydrographic Office.

Kneller, B., Buckee, C., 2000. The structure and fluid mechanics of turbidity currents: A review of some recent studies and their geological implications. Sedimentology 47 (SUPPL. 1), 62–94. http://dx.doi.org/10.1046/j.1365-3091.2000.047s1062.x.

Kozlowski, E.N., 2016. Multi-Scale Forward Modelling of Microbial Lacustrine Carbonates (Ph.d. dissertation). Royal Holloway, University of London, London, p. 401.

Lanteaume, C., Fournier, F., Pellerin, M., Borgomano, J., 2018. Testing geologic assumptions and scenarios in carbonate exploration: insights from integrated stratigraphic, diagenetic, and seismic forward modeling. Lead. Edge 37 (9), 672–680. http://dx.doi.org/10.1190/tle37090672.1.

Lecomte, I., 2008. Resolution and illumination analyses in PSDM: A ray-based approach. Lead. Edge 27 (5), 650–663. http://dx.doi.org/10.1190/1.2919584.

Lecomte, I., Lavadera, P.L., Anell, I., Buckley, S.J., Schmid, D.W., Heeremans, M., 2015. Ray-based seismic modeling of geologic models: Understanding and analyzing seismic images efficiently. Interpretation 3 (4), 71–89. http://dx.doi.org/10.1190/INT-2015-0061.1.

Leeder, M.R., Gawthorpe, R.L., 1987. Sedimentary models for extensional tilt-block/half-graben basins. Geol. Soc. Spec. Publ. 28 (28), 139–152. http://dx.doi.org/10.1144/GSL.SP.1987.028.01.11.

Mandlier, P.G., Kench, P.S., 2012. Analytical modelling of wave refraction and convergence on coral reef platforms: Implications for island formation and stability. Geomorphology 159–160, 84–92. http://dx.doi.org/10.1016/j.geomorph.2012.03.007.

Masiero, I., (in prep.), Ph.d. dissertation, University of Liverpool, Liverpool.

Morley, C.K., Gabdi, S., Seusutthiya, K., 2007. Fault superimposition and linkage resulting from stress changes during rifting: Examples from 3D seismic data, Phitsanulok Basin, Thailand. J. Struct. Geol. 29 (4), 646–663. http://dx.doi.org/10.1016/j.jsg.2006.11.005.

Mouslopoulou, V., Walsh, J.J., Nicol, A., 2009. Fault displacement rates on a range of timescales. Earth Planet. Sci. Lett. 278 (3–4), 186–197. http://dx.doi.org/10.1016/j.epsl.2008.11.031.

Paola, C., 2000. Quantitative models of sedimentary basin filling. Sedimentology 47, 121–178.

Péquignet, A.C., Becker, J.M., Merrifield, M.A., Boc, S.J., 2011. The dissipation of wind wave energy across a fringing reef at ipan, guam. Coral Reefs 30 (SUPPL. 1), 71–82. http://dx.doi.org/10.1007/s00338-011-0719-5.

Pomar, L., 2001. Types of carbonate platforms: A genetic approach. Basin Res. 13 (3), 313–334. http://dx.doi.org/10.1046/j.0950-091X.2001.00152.x.

Pomar, L., Hallock, P., 2008. Carbonate factories: A conundrum in sedimentary geology. Earth-Sci. Rev. 87 (3–4), 134–169. http://dx.doi.org/10.1016/j.earscirev.2007.12.002.

Salles, T., Ding, X., Webster, J.M., Vila-Concejo, A., Brocard, G., Pall, J., 2018. A unified framework for modelling sediment fate from source to sink and its interactions with reef systems over geological times. Sci. Rep. 8 (1), 1–11. http://dx.doi.org/10.1038/s41598-018-23519-8.

Schlagenhauf, A., Manighetti, I., Malavieille, J., Dominguez, S., 2008. Incremental growth of normal faults: Insights from a laser-equipped analog experiment. Earth Planet. Sci. Lett. 273 (3–4), 299–311. http://dx.doi.org/10.1016/j.epsl.2008.06.042.

Schlager, W., 2000. Sedimentation rates and growth potential of tropical, cool water and mud-mound carbonate systems. Geol. Soc. Spec. Publ. 178, 217–227. http://dx.doi.org/10.1144/GSL.SP.2000.178.01.14.

Schlager, W., 2005. Carbonate Sedimentology and Sequence Stratigraphy. The American Association of Petroleum Geologists, p. 200. http://dx.doi.org/10.2110/csp.05.08.

Schlager, W., Reijmer, J.J.G., Droxler, A., 1994. Highstand shedding of Carbonate platforms. SEPM J. Sediment. Res. Vol. 64B, 270–281. http://dx.doi.org/10.1306/D4267FAA-2B26-11D7-8648000102C1865D.

Silvertown, J., Holtier, S., Johnson, J., Dale, P., 1992. Cellular automaton models of interspecific competition for space. J. Ecol. 80 (3), 527–533.

Terray, E.A., Donelan, M.A., Agrawal, Y.C., Drennan, W.M., Kahma, K.K., Williams, A.J., Kitaigorodskii, S.A., 1996. Estimates of kinetic energy dissipation under breaking waves. J. Phys. Oceanogr. 26 (5), 792–807.

Trauth, M.H., 2015. MATLAB registered recipes for earth sciences. p. 288, http://dx.doi.org/10.1007/978-3-540-72749-1 URL papers2://publication/uuid/9EDB56D6-1074-42D3-91B5-677746C89F6C.

Waltham, D., Hardy, S., 1995. The velocity description of deformation. paper 1: theory. Mar. Pet. Geol. 12 (2), 153–163. http://dx.doi.org/10.1016/0264-8172(95)92836-L.

Warrlich, G., Bosence, D., Waltham, D., Wood, C., Boylan, A., Badenas, B., 2008. 3D Stratigraphic forward modelling for analysis and prediction of carbonate platform stratigraphies in exploration and production. Mar. Pet. Geol. 25 (1), 35–58. http://dx.doi.org/10.1016/j.marpetgeo.2007.04.005.

Warrlich, G.M., Waltham, D.A., Bosence, D.W., 2002. Quantifying the sequence stratigraphy and drowning mechanisms of atolls using a new 3-d forward stratigraphic modelling program (carbonate 3D). Basin Res. 14 (3), 379–400. http://dx.doi.org/10.1046/j.1365-2117.2002.00181.x.

Williams, H.D., Burgess, P.M., Wright, V.P., Della Porta, G., Granjeon, D., 2011. Investigating Carbonate platform types: Multiple controls and a continuum of geometries. J. Sediment. Res. 81 (1), 18–37. http://dx.doi.org/10.2110/jsr.2011.6.

Wilson, M.E., Bosence, D.W., Limbong, A., 2000. Tertiary syntectonic carbonate platform development in Indonesia. Sedimentology 47 (2), 395–419. http://dx.doi.org/10.1046/j.1365-3091.2000.00299.x.

Wolfram, S., 2002. A New Kind of Science. Wolfram Media, Inc., p. 414.

Wright, V.P., Burgess, P.M., 2005. The carbonate factory continuum, facies mosaics and microfacies: An appraisal of some of the key concepts underpinning carbonate sedimentology. Facies 51 (1–4), 17–23. http://dx.doi.org/10.1007/s10347-005-0049-6.